**Authors**
Xinlin Li, Zheng Xiang, Binbin Ni, Chen Zhou, Zhengyang Zou, Xudong Gu, Xianguo Zhang, Xiaoxin Zhang, Shenyi Zhang, Pingbing Zuo, Harlan Spence, and Geoffrey Reeves

Ann. Geophys., 34, 493–509, 2016
www.ann-geophys.net/34/493/2016/
doi:10.5194/angeo-34-493-2016


Annales Geophysicae Open Access EGU

# Multi-satellite simultaneous observations of magnetopause and atmospheric losses of radiation belt electrons during an intense solar wind dynamic pressure pulse

**Zheng Xiang[1,2], Binbin Ni[1,2], Chen Zhou[1], Zhengyang Zou[1], Xudong Gu[1], Zhengyu Zhao[1], Xianguo Zhang[2], Xiaoxin Zhang[3], Shenyi Zhang[2], Xinlin Li[4], Pingbing Zuo[2], Harlan Spence[5], and Geoffrey Reeves[6]**

[1]Department of Space Physics, School of Electronic Information, Wuhan University, Wuhan, Hubei, China
[2]State Key Laboratory of Space Weather, National Space Science Center, Chinese Academy of Sciences, Beijing, China
[3]National Space Weather Monitoring and Warning Center, China Meteorological Administration, Beijing, China
[4]Laboratory for Atmospheric and Space Physics, University of Colorado, Boulder, Colorado, USA
[5]Institute for the Study of Earth, Oceans, and Space and Department of Physics, University of New Hampshire, Durham, New Hampshire, USA
[6]Space Science and Applications Group, Los Alamos National Laboratory, Los Alamos, New Mexico, USA

*Correspondence to:* Zheng Xiang (xiangzheng@whu.edu.cn) and Binbin Ni (bbni@whu.edu.cn)

Received: 29 September 2015 – Revised: 18 March 2016 – Accepted: 18 April 2016 – Published: 3 May 2016

**Abstract.** Radiation belt electron flux dropouts are a kind of drastic variation in the Earth's magnetosphere, understanding of which is of both scientific and societal importance. Using electron flux data from a group of 14 satellites, we report multi-satellite simultaneous observations of magnetopause and atmospheric losses of radiation belt electrons during an event of intense solar wind dynamic pressure pulse. When the pulse occurred, magnetopause and atmospheric loss could take effect concurrently contributing to the electron flux dropout. Losses through the magnetopause were observed to be efficient and significant at $L \gtrsim 5$, owing to the magnetopause intrusion into $L \sim 6$ and outward radial diffusion associated with sharp negative gradient in electron phase space density. Losses to the atmosphere were directly identified from the precipitating electron flux observations, for which pitch angle scattering by plasma waves could be mainly responsible. While the convection and substorm injections strongly enhanced the energetic electron fluxes up to hundreds of keV, they could delay other than avoid the occurrence of electron flux dropout at these energies. It is demonstrated that the pulse-time radiation belt electron flux dropout depends strongly on the specific interplanetary and magnetospheric conditions and that losses through the magnetopause and to the atmosphere and enhancements of substorm injection play an essential role in combination, which should be incorporated as a whole into future simulations for comprehending the nature of radiation belt electron flux dropouts.

**Keywords.** Magnetospheric physics (energetic particles precipitating; magnetospheric configuration and dynamics) – space plasma physics (wave-particle interactions)

## 1 Introduction

The Earth's electron radiation belts consist of two zones: the inner belt ($1.2 < L < 2$) remains stable with a long-term slow change with respect to the phases of a solar cycle, and the outer belt ($3 < L < 7$) is characteristically featured by highly dynamic variations on timescales ranging from minutes to years (e.g., Friedel et al., 2002; Reeves et al., 2003; Baker et al., 2014).

One dramatic phenomenon in the outer belt is the electron flux dropout, which, as proposed by Turner et al. (2012b), refers to an event in which the flux of trapped electrons decreases by at least a factor of 50 (or by less than 50 if the flux level drops from some significant level to the instrumental background/noise level) as measured at approximately the same $L$ shell, equatorial pitch angle, and magnetic local time (MLT) by the same spacecraft in a period less than or equal to 24 h. Both adiabatic and non-adiabatic effects occur dur-

ing the course of electron flux variation. While the adiabatic effect, in particular the "Dst effect", which describes the adiabatic response of radiation belt electrons during the main phase of a storm, has been suggested to explain a number of electron flux dropouts (e.g., McIlwain, 1966; Li et al., 1997; Kim and Chan, 1997; Tu and Li, 2011), more attention has been paid to the non-adiabatic effect since this process is irreversible with the presence of a true loss.

There are two major mechanisms that can lead to a permanent loss of radiation belt particles. One is the drift loss through the magnetopause (often called "magnetopause shadowing") and outward radial diffusion associated with increased solar wind dynamic pressure (e.g., Turner et al., 2012a), and the other is the atmospheric precipitation due to resonant wave-particle interactions (e.g., Green et al., 2004). The former can be a phenomenon over a broad range of energy (tens of keV to several MeV), while the latter is strongly dependent on electron energy that can resonate with magnetospheric waves and the wave-induced scattering effect as well. Using multi-satellite measurements, Turner et al. (2012a) clarified that during the main phase of a small, CIR-driven geomagnetic storm on 6 January 2011, the majority of the non-adiabatic loss of outer radiation belt electrons > 300 keV was to the Earth's magnetopause through magnetopause shadowing and subsequent rapid outward radial transport. Hudson et al. (2014) simulated three events of radiation belt flux dropout using the LFM MHD code and clearly showed the inward intrusion of the magnetopause for each event. Most recently, Hwang et al. (2015) investigated an electron flux dropout during a weak storm on 7–8 November 2008. Combining the measurements from multiple satellites with the radiation belt environment model simulations (Fok et al., 2008), they found that relativistic and sub-relativistic electrons showed different features in timing and amount of loss, which could be dominated by either or a combination of magnetopause shadowing and atmospheric loss. By analyzing the dynamics of radiation belt electron phase space density assimilated from four spacecraft during 200 days in 1990 and 1991, Shprits et al. (2012) found that approximately 73 % of the dropout events can be associated with the simultaneous sudden jumps (> 7 nPa over several hours) in the solar wind dynamic pressure, and approximately 15 % could be associated with small jumps or gradual increases in solar wind dynamic pressure. A subsequent study of Ni et al. (2013a) used the measurements from six satellites and the Kalman filtering technique to investigate the radiation belt responses to solar wind dynamic pressure variations in 2002 (solar maximum). They found that 68 % of identified solar wind dynamic pressure pulses correspond to electron phase space density dropout events and that 81 % of identified dropout events are associated with solar wind dynamic pressure sudden jumps (i.e., pulses) or a modest increase, which suggests that losses to the magnetopause alone cannot fully explain radiation belt electron dropouts under evolving solar wind conditions. Green et al. (2004) studied 52 rapid decrease events of > 2 MeV electron flux at the geostationary orbit and through a careful analysis revealed that the identified fast depletion of electron flux is likely due to enhanced precipitation into the atmosphere even though its exact cause is uncertain. A variety of magnetospheric waves, including chorus, plasmaspheric hiss, and EMIC waves, are believed to be capable of driving pitch angle scattering losses of radiation belt electrons into the atmosphere, especially during geomagnetically disturbed times (see the review by Thorne, 2010). Recently, based upon the causal relationship between the efficiency of wave-induced scattering loss and the ratio of precipitated to trapped energetic electron fluxes, a novel physics-based technique has been developed to construct the time-varying, data-driven model of event-specific global distribution of whistler-mode waves (W. Li et al., 2013; Thorne et al., 2013b; Ni et al., 2014a).

Since an event of solar wind dynamic pressure pulse commonly corresponds to an inward displacement of the magnetopause and a disturbed period of geomagnetic activity, it is natural to consider that the above two loss processes may occur simultaneously other than exclusively. Increased resources of in situ radiation belt electron flux measurements from satellites with a broad spatial coverage provide a great opportunity to testify this scenario. The focus of the present study is to investigate the magnetopause and atmospheric losses of radiation belt electrons observed by multiple satellites during a radiation belt dropout event corresponding to a solar wind dynamic pressure pulse on 2 October 2013. The outline of this paper is as follows. We provide the description of the instrumentation and data availability in Sect. 2. Section 3 presents multiple spacecraft observations of a radiation belt flux dropout event, which is further investigated to evaluate the signatures of losses through the magnetopause shadowing followed by the outward radial diffusion and losses to the atmosphere. Section 4 discusses our results and shows simultaneous wave observations to assess their potential connection to the radiation belt electron dropout. We summarize the conclusions in Sect. 5.

## 2 Instrumentation and data availability

In this study simultaneous observations from 14 spacecraft are collected to study the radiation belt electron flux dropout in response to a strong intensification of solar wind dynamic pressure. This group of satellites includes three THEMIS spacecraft (A, D, E; The THEMIS Team, 2008), two Van Allen Probes (A, B; The RBSP-EMFISIS Team, 2012; RBSP-ECT Data Portal, 2012), four NOAA POES spacecraft (POES 15, 16, 18, 19; NOAA, 2013), one GOES spacecraft, three FengYun series spacecraft (2E, 3B, 3C; available upon request to Binbin Ni (bbni@whu.edu.cn)), and one Colorado Student Space Weather Experiment (CSSWE; CDAWeb, 2012) CubeSat. On one hand, POES, CSSWE, and FengYun 3B & 3C spacecraft provide the electron flux

information at low altitudes of hundreds of kilometers. On the other hand, Van Allen Probes, GOES-15 satellite, and FengYun 2E spacecraft provide data of electron distributions in the equatorial region in the inner magnetosphere, and THEMIS spacecraft can extend to the central plasma sheet beyond $L \sim 12$.

While originally designed to measure the upper end of particle distributions for the determination of complete moments and to identify current boundaries, the THEMIS solid state telescope (SST) instrument can provide measurements of near-equatorial energetic electron fluxes from $\sim 30$ to 719 keV with inherent pitch angle resolution of 22.5–37° but interpolated and binned in 5° pitch angle increments (Angelopoulos et al, 2008). In this study, we analyze SST electron flux data from the three innermost THEMIS probes (A, D, and E) with perigees of below 2 $R_E$ and apogees above 10 $R_E$.

The dual-spacecraft Van Allen Probes mission, launched in August 2012 and flying in nearly the same highly elliptical ($1.1 \times 5.8 R_E$), low inclination orbits (Mauk et al., 2012), has provided a new window for looking into the dynamic variations of radiation belt electrons from $\sim 10$ s of keV to 10 s of MeV. Both particle and wave measurements from the twin Van Allen Probes are utilized. The Magnetic Electron Ion Spectrometer (MagEIS) instrument (Blake et al., 2013) of the Energetic Particle, Composition, and Thermal Plasma (ECT) suite (Spence et al., 2013) contains one low-energy unit, two medium-energy units, and a high-energy unit, thereby offering pitch angle resolved energetic electron measurements over the critical energy range of 20 keV to 4.8 MeV. The Relativistic Electron Proton Telescope (REPT) also of the ECT suite is well designed to provide precise and unambiguous directional measurements of ultra-relativistic electron fluxes in the energy range $\sim 1.5$ to 20 MeV (Baker et al., 2013). Besides particle measurements, the Electric and Magnetic Field Instrument Suite and Integrated Science (EMFISIS) provides measurements of DC magnetic fields (magnetometer instrument) and a comprehensive set of wave electric and magnetic fields (Waves instrument) (Kletzing et al., 2013). The Waveform Receiver (WFR) on the EMFISIS Waves instrument measures wave power spectral density from 10 Hz up to 12 kHz (Kletzing et al., 2013), and the High-Frequency Receiver (HFR) provides electric spectral intensity between 10 and 400 kHz, thus enabling measurements of the upper hybrid resonance frequency, from which the total plasma density can be evaluated.

The NOAA POES mission consists of a number of satellites operating simultaneously with good coverage over a broad range of MLT and $L = \sim 2$–8 every $\sim 100$ min. As polar orbiting sun synchronous satellites at an altitude of $\sim 800$ km with an orbital period of $\sim 100$ min, the POES satellites have the SEM-2 instrument package that includes two electron solid-state detector telescopes to measure electron fluxes in three energy bands (> 30, > 100, and > 300 keV) (Evans and Greer, 2004; Green, 2013). The 0° telescope measures precipitating flux inside the bounce loss cone at $L > 1.4$ (Rodger et al., 2010), and the 90° telescope, mounted approximately perpendicular to the 0° telescope, mostly measures the trapped particles between 55 and 68° invariant latitude ($L = \sim 3$–7 in a dipole field) (Meredith et al., 2011). In the present study, we use the Medium Energy Proton and Electron Detector (MEPED) onboard four POES satellites, i.e., NOAA-15, NOAA-16, NOAA18, and NOAA-19. To obtain the clean data sets, we remove the proton contamination using the correction procedure described in Lam et al. (2010), and remove the points during the solar proton events and those measured at the region of the South Atlantic Anomaly (SAA) (Casadio and Arino, 2011).

The NOAA GOES mission consists of a number of geosynchronous orbit (GEO) satellites. GOES-15 was launched in March 2010 and replaced GOES-11 as GOES-WEST in December 2011. The particle detector onboard GOES-15 can provide 1 min resolution data of electron fluxes at three energy channels, i.e., > 0.8, > 2, and > 4 MeV, for the present study.

FengYun 2E is one of a Chinese satellite series at the geosynchronous orbit. Launched in December 2008, FengYun 2E contains a space particle detector that can measure the spin-averaged fluxes for two electron energy channels, i.e., $\geq 0.35$ and $\geq 2$ MeV, with a field of view of 60° (Wang et al., 2008). FengYun 3B and 3C were launched in November 2011 and September 2013, respectively, into the solar synchronization orbit at an altitude of about 800 km with an inclination of 98°. Both satellites contain the detector to provide the electron fluxes for five energy channels between 0.15 and 5.7 MeV. With a field of view of 40° for electron measurements, the detector is mounted perpendicular to the plane of the satellite trajectory and therefore mainly monitors the trapped population of energetic electrons (Wang et al., 2010, 2013).

The Colorado Student Space Weather Experiment (CSSWE) was launched into a highly inclined (65°) low Earth orbit (480 km × 780 km) in September 2012 (Li et al., 2012, 2013a, b). The Relativistic Electron Proton Telescope integrated little experiment (REPTile) was the only science payload onboard CSSWE, which was designed to measure the relativistic electron fluxes for three energy channels, i.e., 0.58–1.63, 1.63–3.8, and > 3.8 MeV. CSSWE traverses the radiation belts four times in each orbit ($\sim 90$ min), providing a global view of their spatial structure. Electrons that can be measured by REPTile can be separated into three categories of trapped, quasi-trapped, and untrapped population in terms of the satellite location and the geometry of ambient magnetic field (e.g., the South Atlantic Anomaly).

The present study is aimed at investigating the abrupt response of the electron radiation belt to a solar wind dynamic pressure pulse event that occurred at 02:00–05:00 UT on 2 October 2013. Figure 1 shows the corresponding solar wind parameters and geomagnetic indices obtained from the OMNIWeb. Panels, from top to bottom, present the temporal

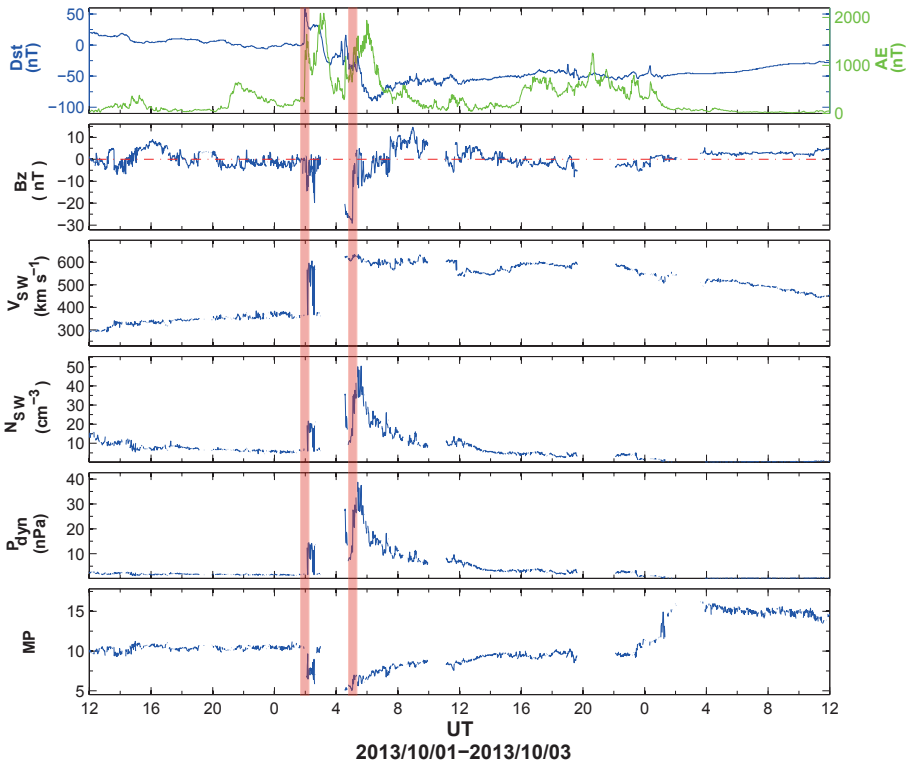


**Figure 1.** Time series of OMNIWeb geomagnetic indices and solar wind parameters for the 2-day interval between 12:00 UT on 1 October and 12:00 UT on 3 October, 2013. From top to bottom: Dst and AE, IMF $B_z$, solar wind speed ($V_{sw}$), solar wind proton density ($N_{sw}$), solar wind dynamic pressure ($P_{dyn}$), and the magnetopause standoff distance modeled following Shue et al. (1997). The two vertical lines denote the start time of the two intense $P_{dyn}$ enhancements during the intense solar wind dynamic pressure pulse.

variations of the Dst index, AE index, interplanetary magnetic field (IMF) $B_z$, solar wind speed $V_{sw}$, solar wind proton density $N_{sw}$, solar wind dynamic pressure $P_{dyn}$, and magnetopause standoff distance based on Shue et al. (1997), respectively. During the data gap of ∼ 03:00–04:00 UT on 2 October 2013 for the OMNIWeb data sets, these parameters had no significant changes based on the WIND measurements, which are provided in the Supplement. Obviously, two $P_{dyn}$ intensification occurred between 02:00 and 06:00 UT. The first was featured with an increase of over 10 nPa within 0.5 h, and the second with an increase of ∼ 30 nPa within 1 h, as indicated by the two vertical dashed lines. Concurrently, IMF $B_z$ was strongly southward, reaching a minimum of ∼ −30 nT; $V_{sw}$ jumped from ∼ 350 to > 600 km s$^{-1}$; $N_{sw}$ increased from ∼ 10 to > 50 cm$^{-3}$, showing a variation trend very similar to $P_{dyn}$; the magnetopause was substantially compressed inwards to a location as low as ∼ 5 $R_E$. In addition, the geomagnetic activity was highly disturbed, manifesting an obvious sudden storm commencement (SSC) above 50 nT, a moderately strong geomagnetic storm with $(Dst)_{min}$ ∼ −90 nT, and a remarkably fluctuated profile of AE index with the maximum over 2000 nT. After the pulse event, while $V_{sw}$ remained high, $P_{dyn}$ dropped quickly within 5 h. In addition, the geomagnetic storm evolved into the recovery phase and the location of the magnetopause retreated rapidly to ∼ 10 $R_E$ and beyond. During the period of the dynamic pressure pulse, GOES 13 was approximately on the nightside (21:00–00:00 MLT) to see the substorm injections of both electrons (40–475 keV) and protons (95–575) corresponding to the dynamic pressure enhancements and increase of AE index, the results of which are shown in Fig. 2.

Figure 3 illustrates the satellite trajectories during 02:00–14:00 UT on 2 October 2013 for four NOAA POES satellites, GOES-15, three innermost THEMIS probes (A, D, E), and two NASA Van Allen probes in the GSM $x$-$y$ plane. It is clearly seen that the satellite constellation covered a wide range of both MLT and $L$ shell, thereby providing a good opportunity to investigate the magnetospheric response to the occurrence of $P_{dyn}$ pulse.

## 3 Multi-satellite observations of a radiation belt electron flux dropout

In this section, we illustrate in situ observations of a radiation belt flux dropout event. We further investigate simultaneous electron flux measurements from multiple satellites, aiming towards an overall representation of the major loss mecha-

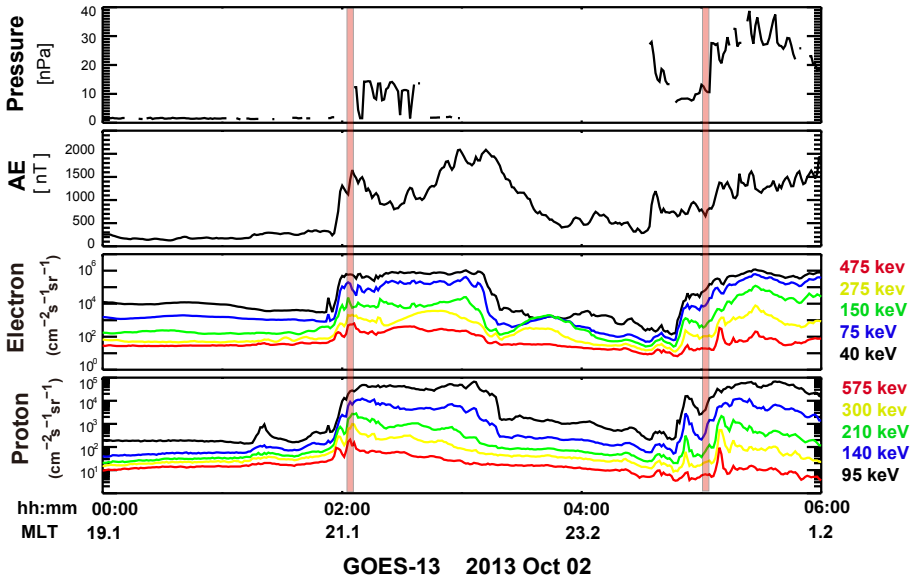


**Figure 2.** Time series of electron and proton fluxes observed by GOES-13 between 00:00 and 06:00 UT on 2 October 2013. From top to bottom: solar wind dynamic pressure, AE index, electron fluxes of five color-coded energy channels, and proton fluxes of five color-coded energy channels. The two vertical lines present the two intense $P_{dyn}$ enhancements.

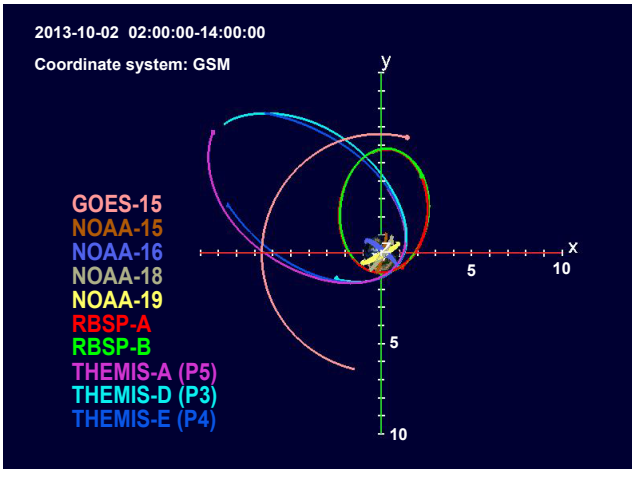


**Figure 3.** Satellite trajectories during 02:00–14:00 UT on 2 October 2013 for four NOAA POES satellites, GOES-15, three innermost THEMIS probes (A, D, E), and two NASA Van Allen probes in the GSM $x$-$y$ plane.

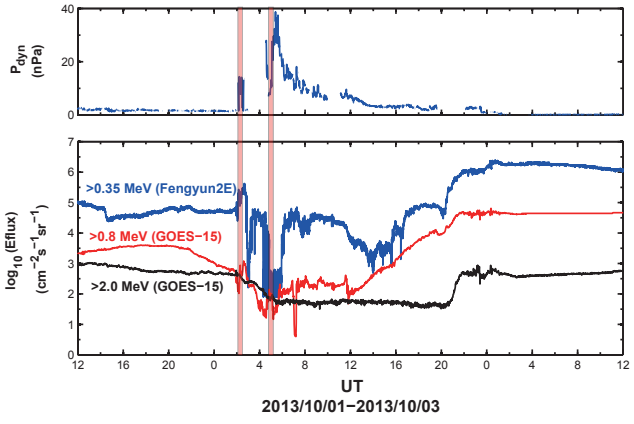


**Figure 4.** (top) Temporal variations of $P_{dyn}$. (bottom) Observations of radiation belt electron fluxes at the geostationary orbit by two satellites, i.e., GOES-15 and FengYun 2E, for three specific energy channels: (blue) > 0.35 MeV, (red) > 0.8 MeV, and (black) > 2 MeV. The two vertical lines denote the start time of the two intense $P_{dyn}$ enhancements.

nisms in association with magnetopause shadowing and atmospheric precipitation.

### 3.1 Identification of a flux dropout event

Figure 4 shows the observations of radiation belt electron fluxes at the geostationary orbit by two satellites, i.e., GOES-15 and FengYun 2E. The blue curve displays the temporal flux variation of > 0.35 MeV electrons observed by FengYun 2E, and the red and black curves display GOES-15 observed temporal flux variations of > 0.8 and > 2 MeV electrons, respectively. The start times of two intense $P_{dyn}$ enhancements are indicated by the two vertical lines. Overall, the flux dropout occurred remarkably for the electron energy channels of > 0.35 and > 0.8 MeV but less pronouncedly for > 2 MeV electrons.

Specifically, during the first $P_{dyn}$ enhancement, the fluxes of > 0.35 MeV electrons initially increased by a factor of ∼ 3 within an hour and then dropped substantially by over 3 orders of magnitude within another hour. The fluxes of

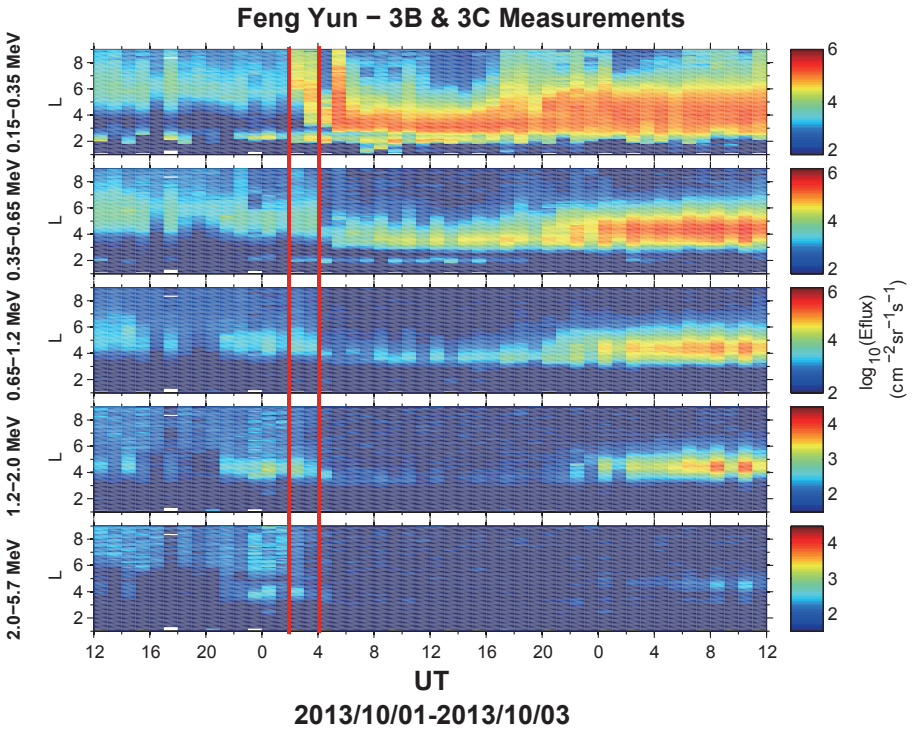


**Figure 5.** Temporal variations of radiation belt electron flux observed by low-altitude FengYun 3B and 3C spacecraft during the 2-day period for five energy channels, i.e., 0.15–0.35, 0.35–0.65-, 0.65–1.2, 1.2–2, and 2–5.7 MeV. The two vertical lines represent the start of the two intense $P_{dyn}$ enhancements. The color scale specifies the logarithmic values of electron fluxes.

> 0.8 MeV electrons showed a similar trend of temporal evolution but to a lesser extent of change. A possible explanation is that strongly enhanced substorm activities (Fig. 2) produced the large increase in electron population of hundreds of keV at the early stage, which subsequently underwent efficient loss processes to account for substantial drops in the electron flux. When the second intense $P_{dyn}$ enhancement occurred, the substorm activities remained active. However, the fluxes of > 0.35 MeV electrons decreased almost concurrently by over 2 orders of magnitude and lasted for over an hour before the restoration to the pre-storm level, probably due to the fact that the second $P_{dyn}$ enhancement was stronger than the first one and the energetic particle was weaker as well. It is also seen that about 18 h after the second $P_{dyn}$ enhancement the electron fluxes at all indicated energy channels reached a quite stable state comparable to or higher than the pre-storm (i.e., pre-pulse) level.

The above radiation belt electron flux dropouts at the geosynchronous orbit are apparently associated with the enhancements of $P_{dyn}$ and the evolvement of a moderately strong geomagnetic storm also developed (first panel of Fig. 1). Qualitatively, the overall changes of the geosynchronous electron fluxes are most likely to reflect a combination of adiabatic (reversible) and non-adiabatic (irreversible) variations. On the one hand, the typical Dst effect may at least partly contribute to the fast recovery of > 0.35 MeV electron fluxes after the first $P_{dyn}$ enhancement. On the other hand, in situ measurements from other satellites with a broad spatial coverage can bring essential information to understand the physical processes that can result in real losses, which will be investigated comprehensively in the following subsections.

### 3.2 Observations of losses through the magnetopause

Figure 5 shows an overview of the radiation belt electron variations observed by low-altitude FengYun 3B and 3C spacecraft during a 2-day period from 1 to 3 October. Binned by 0.1 $L$ shell with a time resolution of 1 h, the fluxes of trapped electrons are displayed for five energy channels, i.e., 0.15–0.35, 0.35–0.65, 0.65–1.2, 1.2–2, and 2–6.5 MeV. The two vertical lines represent the start of the two intense $P_{dyn}$ enhancements. The observed electron flux dropout occurred for almost all the energy channels after the second Pdyn enhancement, principally at the spatial extents of $L \gtrsim 5$, which is consistent with the inward penetration of the standoff distance of the magnetopause to $\sim 5\,R_E$ (Fig. 1) in response to the solar wind dynamic pressure pulse. A very likely explanation for this overall profile over a broad energy range is that the electron population that initially drift on a closed trajectory find themselves on an open drift shell where they encounter the magnetopause on the dayside and get lost through this outer boundary sink into the magnetosheath (e.g., Millan

and Thorne, 2007; Turner et al., 2012a, b). The effect of magnetopause shadowing can produce a sharp gradient in the radial distribution of electron phase space density and thereby drive outward radial diffusion that potentially reduces the outer zone electron fluxes efficiently in a few hours (e.g., Shprits et al., 2006). Consequently, the flux dropout was seen to extend to lower $L$ shells (i.e., $L \sim 4$) for 1.2–2.0 and 2.0–5.7 MeV energy channels right after the second $P_{\rm dyn}$ pulse. Consequently, a significant scenario for this event is that the effect of magnetopause shadowing is directly effective to remove electron down to $L \sim 5$ and subsequent outward radial diffusion becomes important to drive substantial losses of outer radiation belt electrons down to even lower $L$ shells.

Notably, the electron fluxes at $L \gtrsim 5$ responded differently to the two $P_{\rm dyn}$ enhancements. During the period of the first enhancement, 0.15–0.35 and 0.35–0.65 MeV electron fluxes did not exhibit decrease but increase, while 1.2–2.0 and 2.0–5.7 MeV electron fluxes showed a slight decrease. When the second (more intense) $P_{\rm dyn}$ enhancements occurred, electron fluxes >0.35 MeV were uniformly low as a result of real losses, however, electron fluxes of 0.15–0.35 MeV initially decreased remarkably within an hour, subsequently increased dramatically in the following hour, and then decreased substantially again for several hours. Clearly, enhanced convection and injection during magnetic substorms is an important factor to affect the responses of radiation belt electrons to a strong dynamic pressure pulse. Specifically, it tends to cause electron flux increases other than decreases at energies below hundreds of keV (Li et al., 2002). It is also interesting to see the differences in the energy components, flux magnitude, and innermost penetration region of injected electrons between the two $P_{\rm dyn}$ enhancements, which imply the strong dependence of storm-time outer zone electron flux evolution on the specific interplanetary and magnetospheric conditions.

While the electron flux dropout remained present after the decay of the dynamic pressure pulse, in particular at $L \gtrsim 5$, 0.15–0.35 MeV electron fluxes recovered most quickly within 12 h, accompanied by substorm activities. In contrast, higher energy electrons took much longer time (> 1 day) for recovery to the pre-pulse level (Thorne et al., 2013b; Boyd et al., 2014]. Post-pulse electron flux build-ups initially occurred at $L \sim 4$–5 with a relatively small extent of increase, and subsequently expanded to both lower and higher $L$ shells with much larger enhancements. The distinct timing and magnitude of the flux increase with respect to electron energy strongly suggests the essential contribution that resonant wave-particle interactions made in the storm recovery phase to the dynamic evolution of radiation belt electrons.

Observations of trapped radiation belt electron flux in the equatorial region are obtained from the MagEIS and REPT instrument onboard Van Allen Probes and SST instrument onboard THEMIS A, D, and E, the results of which are shown in Fig. 6. The first four panels show the SST data of radiation belt energetic electrons at four specified energies, i.e., 31, 139, 408, and 720 keV, the middle three panels show the MagEIS data at three specified energies, i.e., 110, 590, and 1200 keV, and the bottom three panels show the REPT data at highly relativistic energies, i.e., 2.3, 3.6, and 4.5 MeV. The two vertical lines correspond to the start time of the two intense $P_{\rm dyn}$ enhancements. The horizontal lines with arrows indicate the time intervals of observed electron flux dropouts.

According to THEMIS measurements, the dramatic electron losses after the second pressure enhancement were obvious for 31 and 139 keV electrons at very high $L$ shells, e.g., $L \gtrsim 8$, close to the outer magnetospheric boundary, which is a strong signature of magnetopause shadowing. The real electron losses lasted for at least 12 h, and extended to $L \sim 6$ which could be attributed to the outward radial diffusion. During the late recovery phase after the decay of the dynamic pressure pulse, magnetospheric electron fluxes reached or exceeded the pre-pulse level, indicating the occurrence of acceleration processes. However, the flux variations at energies of 408 and 702 keV were faint with respect to the dynamic pressure pulse. One possible reason is that the flux values are generally very small for these energies at high $L$ shells so that large decrease in electron flux cannot be evidently discerned. Potential proton interfere of SST electron fluxes at higher energies might also take effect, or just due to instruments saturation ($L < 5$). Twin Van Allen Probes MagEIS observations show that there tends to be no decrease in energetic electron flux for 110 keV, which can be reasonably explained as a result of enhanced convective injection, consistent with the flux observations at the geostationary orbit as shown in Figs. 2 and 4. Large drops in electron flux primarily occurred for 590 keV and 1.2 MeV. By comparison, the flux decreases occurred at $L \gtrsim 4.5$ for 590 keV but extended to lower locations of $L < 4$ for 1.2 MeV. The recovery time required to restore the pre-pulse flux level was $\sim 3$ and $\sim 12$ h, respectively. REPT flux observations manifest interesting features of ultra-relativistic electron loss in response to an intense dynamic pressure pulse. While it is difficult to distinguish the flux variations at the spacecraft apogee, i.e., $L \sim 6$, and for electrons $\geq 4.5$ MeV (since their flux values are very small), the large flux decreases were apparent at $L = 3$–4 for 2.3 and 3.6 MeV electrons. These drops in electron flux lasted for $\sim 15$ h and even longer.

To better distinguish between the adiabatic and non-adiabatic changes in radiation belt electron distribution, we compute electron phase space densities (PSD) in the phase space coordinate defined by the three adiabatic invariants ($\mu$, $K$, and $L^*$) following the methodology of Ni et al. (2009a, b). Three data sets of pitch angle resolved electron fluxes measured from THEMIS SST and Van Allen Probes MagEIS and REPT instrument are adopted to evaluate the radial profile of electron PSD. Note that $L^*$-values for Van Allen Probes and THEMIS are computed using the TS04s model (Tsyganenko and Sitnov, 2005). Figure 7 shows the results of electron PSDs for THEMIS and Van Allen Probes corresponding to a fixed value of $K = 0.05 G^{1/2} R_{\rm E}$ and a group of $\mu$ val-

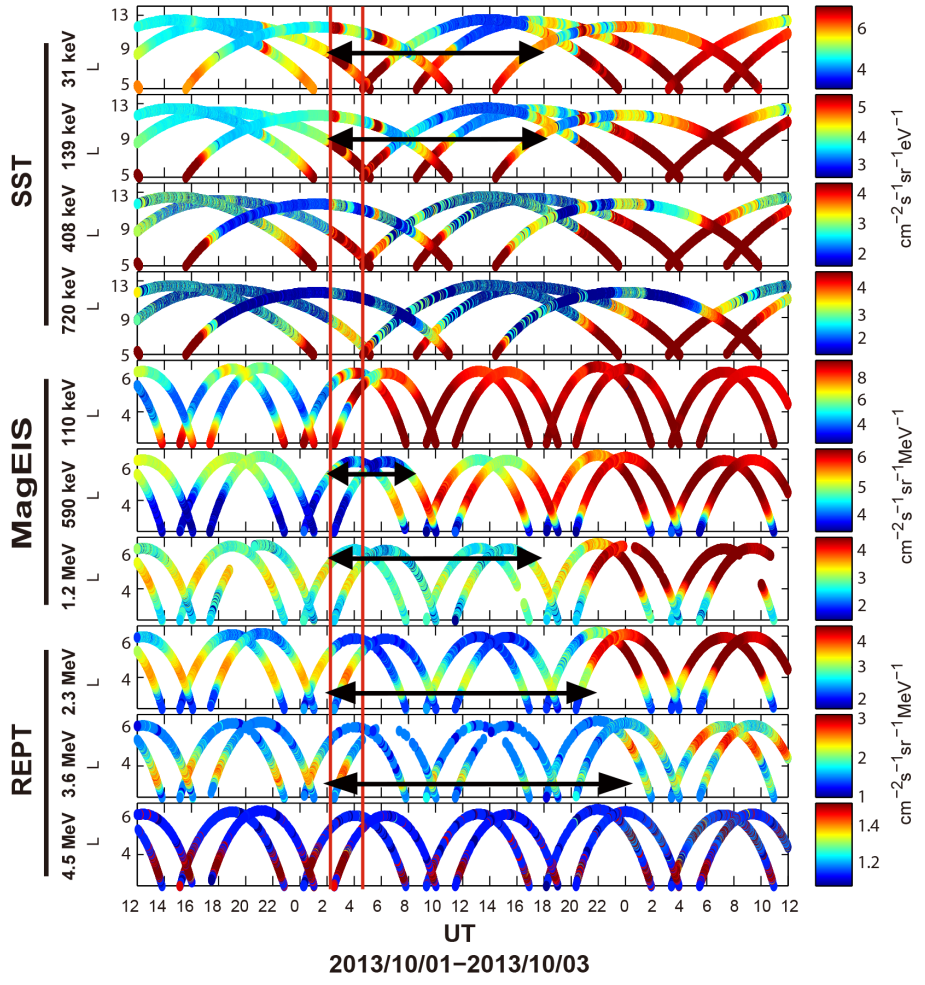


**Figure 6.** Temporal variations of radiation belt electron flux observed by the SST instrument onboard THEMIS A, D, E from $L = 5$ to $L = 14$ and the MagEIS and REPT instrument onboard Van Allen Probes between $L = 2.5$ and $L = 6.5$ during the 2-day period for the indicated 10 energy channels. The two vertical lines represent the start of the two intense $P_{\mathrm{dyn}}$ enhancements. The color scale specifies the logarithmic values of electron fluxes.

ues. The red lines indicate the start time of the Pdyn pulses. The data gap of PSD for THEMIS at higher $L^*$-values is due to the fact that the satellite(s) moved outside the magnetopause to intersect with an open field line. For Van Allen Probes, $L^*$ becomes unavailable particularly during the pressure pulse period when the magnetopause was highly compressed to much lower $L$ shells for which the last closed drift shell was pushed substantially inwards. When the first $P_{\mathrm{dyn}}$ pulse occurred, substorm injections were obvious at $L^* \sim 7$ from the THEMIS measurements, as indicated in the first two panels. ForVan Allen Probes measurements, $L^*$-values show dramatic variations following the storm sudden commencement (denoted by the first red vertical line). After the second $P_{\mathrm{dyn}}$ pulse, Van Allen Probes captured substantial decrease of electron PSD at higher $\mu$-values, especially when $\mu \geq 500\,\mathrm{MeV\,G^{-1}}$ that corresponds to $\gtrsim 1\,\mathrm{MeV}$ electrons at $L^* < 4$. Since the magnetopause was rather "distant" at $L^* < 4$, we suggest that those real losses of highly relativistic electrons near the heart of the outer radiation belt were mainly due to the atmospheric precipitation. In addition, outward radial transport following the magnetopause shadowing and/or negative gradient in electron phase space density could be also effective down to $L^* = 4$ (e.g., Turner et al., 2014a). To clarify it quantitatively needs full dynamic modeling of the magnetic field during the main phase of the storm, which however is beyond the scope of this paper. The process of atmospheric losses from the outer radiation belt can be triggered via pitch angle scattering by a variety of magnetospheric waves such as whistler-mode chorus, plasmaspheric hiss, and EMIC waves (e.g., Summers et al., 2007; Thorne, 2010), which is outside the scope of the present study but will be discussed in next section. It is also worthwhile to point out that the combined measurements from THEMIS and Van Allen Probes consistently show the flux decreases with a broad spatial coverage from $L \gtrsim 10$ to $L \lesssim 5$. It implies that outward radial diffusion in addition to magnetopause shad-

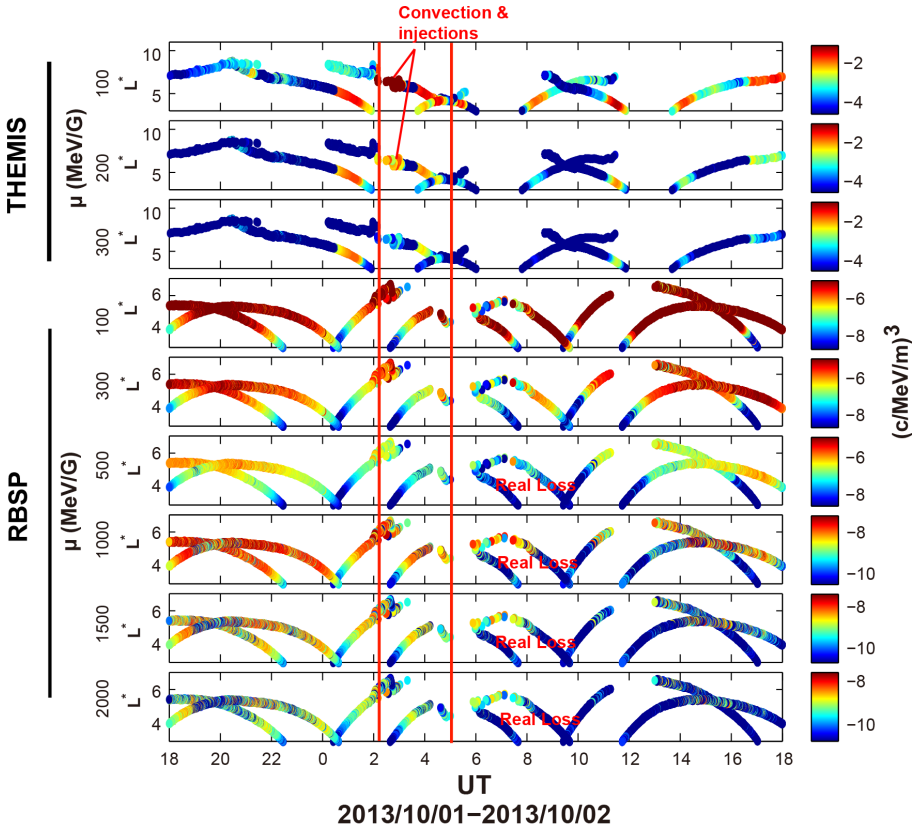


**Figure 7.** Computed electron PSDs for THEMIS and Van Allen Probes corresponding to a fixed value of $K = 0.05G^{1/2}\,R_E$ and a group of $\mu$ values. The red lines indicate the start time of $P_{dyn}$ pulses. The calculations of $L^*$ are performed using the TS04s geomagnetic field model.

owing contribute to the fast and significant depletion of both energetic and relativistic electrons in the magnetosphere.

### 3.3 Observations of losses to the atmosphere

Measurements of precipitating electron fluxes from low-altitude POES spacecraft are critical to investigate the atmospheric loss of radiation belt electrons. Figure 8 shows the profiles of precipitated and trapped electron fluxes measured by the MEPED instrument onboard four POES satellites, i.e., NOAA-15, NOAA-16, NOAA-18, and NOAA-19, for the indicated three energy channels (> 30, > 100, and > 300 keV). The data are binned by every 0.1 $L$ and every 0.5 h for the 2-day period of interest. The two vertical lines correspond to the start time of the two intense $P_{dyn}$ enhancements.

Electron precipitation into the atmosphere was evident for all three energy channels for a broad coverage of $L$ shell, say, $L > 3$. The electron precipitation fluxes maximized during the period of enhanced substorm injection. When the dynamic pressure pulse evolved, the fluxes became smaller but clearly observed, demonstrating a continuous presence of outer zone electrons in either bounce or drift loss cone for precipitation losses. Combining the precipitated and trapped electron fluxes together, we see that within 1 day of the pulse occurrence the two flux profiles at $L \gtrsim 4.5$ showed a similar variation tendency in response to the interplanetary and geomagnetic conditions. We note that decreases in the trapped electron fluxes can be partially explained by the observations of precipitated electrons, since the total electron population at all pitch angles dropped markedly after the occurrence of the dynamic pressure pulse, which supports the above-mentioned hypothesis of magnetopause shadowing and outward radial diffusion. The enhancements of the trapped electron population initially occurred at $L \sim 3$–4 and then expanded to higher $L$ shells quickly during the storm recovery phase, while the corresponding loss processes became less significant. Very likely, wave scattering can primarily account for both the continuous atmospheric loss of precipitating electrons and the considerable energization of trapped electrons, while the responsible magnetospheric waves may be different.

Another data source used to identify the atmospheric loss comes from REPTile onboard CSSWE. Based on REPTile's position versus the International Geomagnetic Reference Field (IGRF) model and assuming that electrons are locally mirroring and that an electron will be lost if it reaches 100 km altitude (Li et al., 2013b), REPTile observed electron fluxes are carefully separated into three groups (based on where the

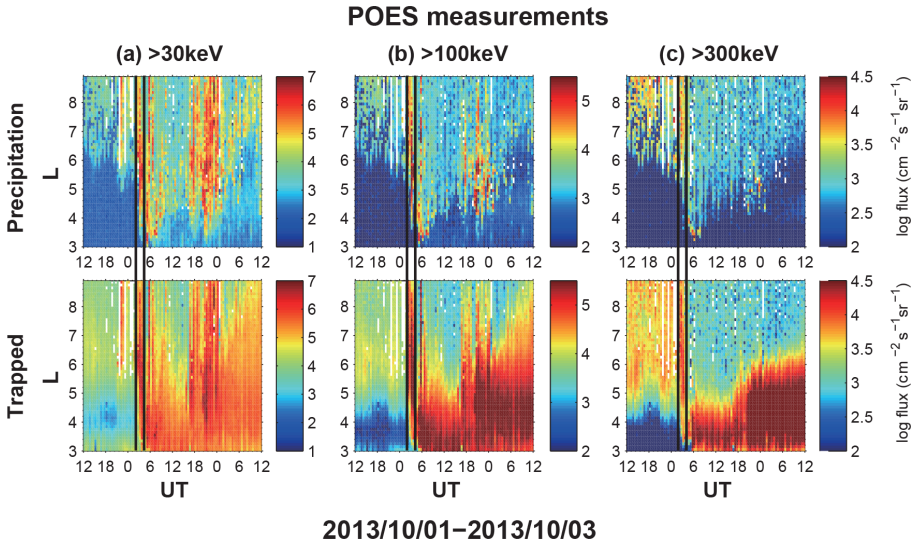


**Figure 8.** Temporal variations of (top) precipitated and (bottom) trapped electron fluxes measured by the MEPED instrument onboard four NOAA POES satellites, i.e., NOAA-15, NOAA-16, NOAA-18, and NOAA-19, for the indicated three energy channels (> 30, > 100, and > 300 keV). The two vertical lines represent the start of the two intense $P_{\mathrm{dyn}}$ enhancements. The color scale specifies the logarithmic values of electron fluxes.

measurements were made) of untrapped population that was measured in the bounce loss cone to precipitate at its conjugate point, quasi-trapped population that was measured in the drift loss cone to lose at the SAA, and trapped population otherwise. Figure 9 shows the fluxes of three electron populations obtained by REPTile during the 3-day period. For the energy channel of 0.58–1.63 MeV, it is clear to capture the increases in precipitating electron fluxes at $L \sim 3.5$–$5.5$ after the dynamic pressure pulse occurred, owing to enhanced losses to the atmosphere. Compared to the measurements 1 day before and after the dynamic pressure pulse event, fluxes of trapped electrons consistently displayed large drops at $L \gtrsim 4.5$ and peaked at lower locations down to $L \sim 3.5$. In contrast, 1.63–3.8 MeV electrons showed nearly no change in the precipitation flux and underwent smaller variations in the quasi-trapped and trapped population.

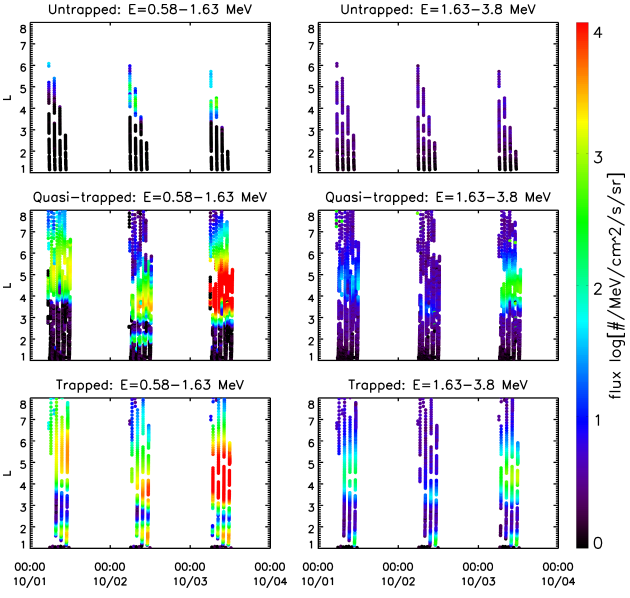


**Figure 9.** Flux variations of three electron populations (from top to bottom: untrapped, quasi-trapped, and trapped) measured by REPTile onboard CSWWE for the energy channels of (left) 0.58–1.63 MeV and (right) 1.63–3.8 MeV during the 3-day period. The color scale specifies the logarithmic values of electron fluxes.The large data gaps are due to limited duty cycle of REPTile during this time period.

## 4 Discussions

The dynamic evolution of magnetospheric electron fluxes is a delicate balance of competing source and loss mechanisms (Reeves et al., 2003; Turner et al., 2014a, b). The source mechanisms include plasma sheet electron injections and wave-induced momentum energization, while loss mechanisms include magnetopause shadowing followed by outward transport and wave-induced pitch angle scatting. As a magnetospheric phenomenon featured as remarkable losses, radiation belt flux dropouts were first thought as a result of purely adiabatic, reversible effects (Dessler and Karplus, 1961), which was later recognized to break down when real electron losses occur during geomagnetic storms and/or associated with solar wind dynamic pressure increase (see the review of Millan and Thorne (2007) and the references therein). In the present study, direct measurements of electron fluxes are adopted to analyze the flux dropout profiles

**Table 1.** A list showing the electron loss feature observed by each satellite and the corresponding possible cause(s).

| Satellites | Observed loss | Possible loss cause(s) |
|---|---|---|
| THEMIS A & D & E | loss at high $L \gtrsim 7$<br>31–139 keV | Magnetopause shadowing and<br>outward radial diffusion |
| Van Allen Probes<br>A & B | (1) loss at $L \gtrsim 5$;<br>110 keV–3.6 MeV<br>(2) loss at $L = 3$–4 | (1) outward radial diffusion associated<br>with magnetopause shadowing<br>(2) wave scattering |
| NOAA 15, 16, 18, 19 | (1) enhanced precipitation to the<br>atmosphere at $L > 3$<br>(2) decrease in trapped population at higher<br>$L$ shells; > 30 to > 300 keV | (1) wave scattering<br><br>(2) magnetopause shadowing followed<br>by outward radial diffusion |
| GOES 15 | Large loss<br>> 0.8 and > 2.0 MeV | Magnetopause shadowing and<br>outward radial diffusion |
| FengYun 2E | Large loss<br>> 0.35 MeV | Magnetopause shadowing and<br>outward radial diffusion |
| FengYun 3B & 3C | decrease in trapped population<br>at $L \gtrsim 5$; 0.15–2.7 MeV | Magnetopause shadowing and<br>outward radial diffusion |
| CSWWE | (1) enhanced precipitation to<br>the atmosphere at $L > 4$<br>(2) decrease in trapped population at<br>$L \gtrsim 5$; 0.58–3.8 MeV | (1) wave scattering<br><br>(2) magnetopause shadowing and<br>outward radial diffusion |

and to investigate the underlying physical processes of loss during an intense solar wind dynamic pressure pulse. Basically, adoption of electron fluxes cannot rule out the adiabatic effect that mixes with the non-adiabatic effects. Specifically, here the adiabatic effect refers to the Dst effect which is closely associated with the variations of the ambient magnetic field intensity and its geometry, and the non-adiabatic effects refer to losses to the magnetopause and to the atmosphere. To accurately determine the driver(s) of observed dynamics, it is important to convert electron fluxes to electron phase space densities (PSD) as a function of the three adiabatic invariants (e.g., Chen et al., 2007; Ni et al., 2013a), which however requires pitch angle resolved flux information as a function of kinetic energy and a reliable model of the ambient magnetic field. Therefore, various assumptions should be made to evaluate electron PSD. In the present study, except THEMIS and Van Allen Probes, all the other satellites cannot provide the information of pitch angle distribution, which thereby brings substantial restrictions to electron PSD computations. Furthermore, the combined analyses of simultaneous multiple-satellite measurements have great potential to minimize the deficiency of using flux data to identify and understand real losses of radiation belt electrons from various perspectives of view, e.g., at both low and high altitudes and at both equatorial and high latitudes. Therefore, we argue that it is feasible to utilize the electron flux data from 14 satellites and PSD from THEMIS and Van Allen Probes to look into the loss processes of the electron flux dropout during the dynamic pressure pulse event on 2 October 2013.

A major and significant impression that we obtain concerning electron losses from the simultaneous flux observations by multiple satellites is that when an intense dynamic pressure pulse occurs, losses through the magnetopause (magnetopause shadowing) and to the atmosphere can take effect concurrently and each satellite, depending on its location, can act as witness to one or both physical processes connecting to the real depletion of electron fluxes. A general picture is that in response to the dynamic pressure pulse event and geomagnetic storm on 2 October 2013, losses through the magnetopause were efficient and significant at $L \gtrsim 10$, which was captured by THEMIS spacecraft around the magnetospheric outer boundary. The resultant sharp negative gradient in electron distribution at large $L$ shells contributed to enhanced losses at $L$ shells down to $L \sim 6$ that resulted from the outward radial diffusion, which could be primarily captured by THEMIS, Van Allen Probes, FengYun, GOES-15, and POES satellites. Losses to the atmosphere were directly identified from the precipitating electron flux observations by POES and CSSWE. It was also manifested as large decreases in trapped electron fluxes around the heart of the outer radiation belt measured by Van Allen Probes. As a summary, Table 1 outlines the main features of the electron losses observed by each satellite and the corresponding possible physical causes. It is noted that the present study cannot distinguish the exact roles that the above two major

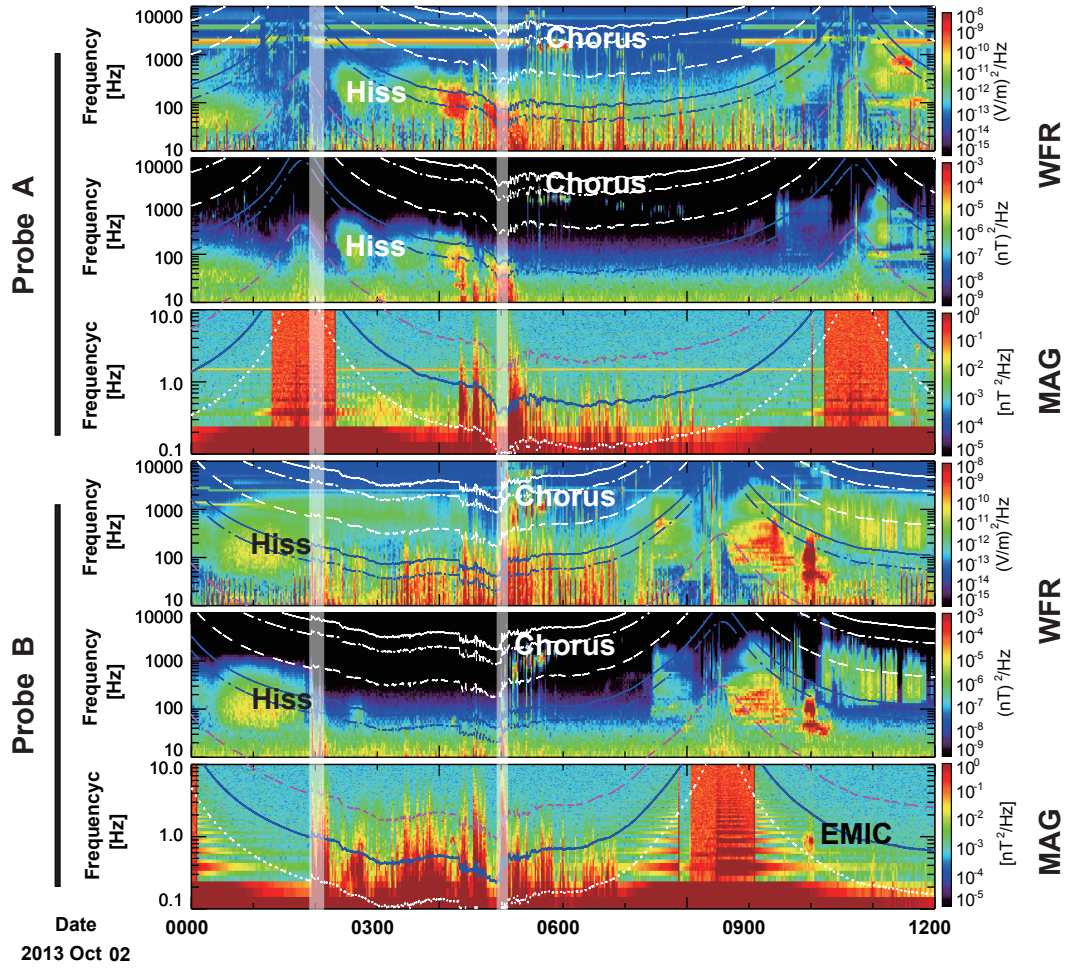


**Figure 10.** Corresponding to the radiation belt electron flux measurements, Van Allen Probes EMFISIS Wide-Frequency Receiver (WFR) observations of electric and magnetic field spectral intensity at 10 Hz–10 kHz and Fluxgate Magnetometer (MAG) observations of electric field spectral intensity at 0.1–10 Hz. The overplotted curves in the WFR spectrograms, from top to bottom, denotes the electron $f_{ce}$, $0.5f_{ce}$, $0.1f_{ce}$, $f_{LHR}$, $0.5f_{LHR}$, and $f_{cp}$, respectively, where $f_{ce}$, $f_{LHR}$ and $f_{cp}$ represent equatorial electron cyclotron frequency, lower hybrid resonance (LHR) frequency, and proton cyclotron frequency. The overplotted curves in the MAG spectrograms denote the local $H^+$, $He^+$ and $O^+$ ion gyrofrequencies, respectively. The two vertical lines represent the start of the two intense $P_{dyn}$ enhancements, and a number of activities of chorus, hiss, and EMIC waves are labeled.

loss mechanisms played in driving the temporal evolution of energetic and relativistic electrons observed by the group of 14 satellites, which however requires future investigation.

While a number of mechanisms are able to result in the atmospheric loss of magnetospheric electrons via transport of previously trapped electrons into the bounce or drift loss cones, we think that pitch angle scattering by plasma waves can be a viable candidate to be mainly responsible for the observed precipitating electron losses for the dynamic pressure pulse event. Firstly, whistler mode chorus can cause efficient pitch angle scattering of electrons into the loss cone leading to precipitation into the atmosphere and net losses of energetic electrons from the outer radiation belt on a timescale of $\sim$ 1 day or less. Thorne et al. (2005) found that chorus driven cyclotron resonance could be responsible for the microbursts of relativistic electron precipitation observed by SAMPEX on the dayside, while Orlova and Shprits (2010) showed that in the realistic magnetosphere chorus waves could also explain the nightside microburst precipitation. Chorus waves are also mainly responsible for the electron diffuse auroral precipitation at $\sim$ 1 keV (Thorne et al., 2010; Ni et al., 2011, 2014b). Secondly, plasmaspheric hiss induced pitch angle scattering of energetic electrons is responsible for the formation of the quiet time slot region that separates the inner and outer radiation belts (Lyons and Thorne, 1973). It also contributes to the slow decay and resultant scattering loss to the atmosphere of relativistic electrons generated during magnetic storms (e.g., Summers et al., 2007; Meredith et al., 2009; Thorne et al., 2013a; Ni et al., 2013b) on a timescale of several days or longer. Apart from inducing direct precip-

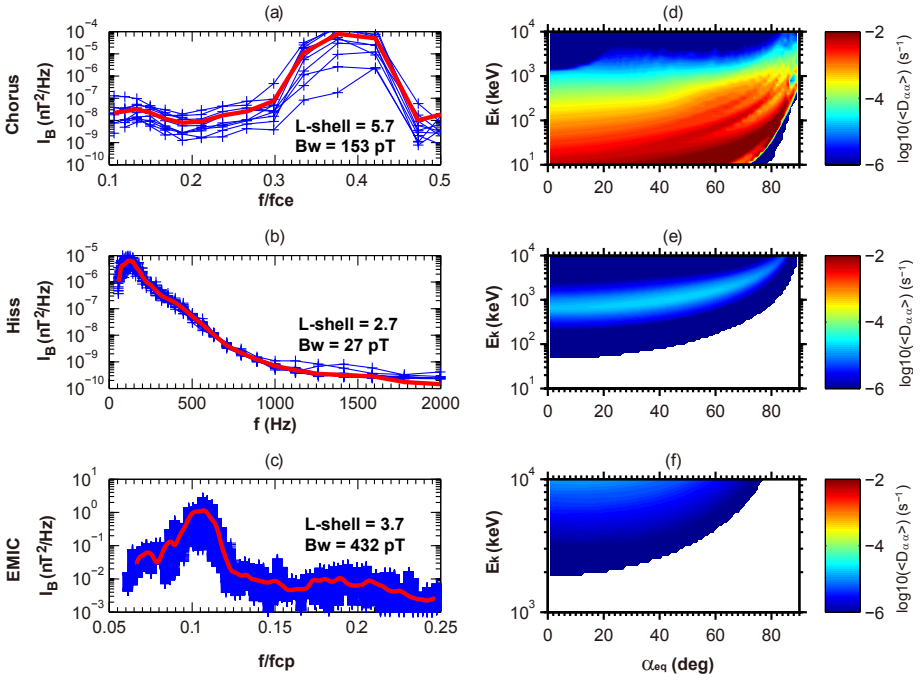


**Figure 11.** Line plots of magnetic field spectral intensity for **(a)** chorus, **(b)** plasmaspheric hiss, and **(c)** $He^+$-band EMIC waves corresponding to the representative periods marked in Fig. 9, together with the mean profiles shown as thick red curves. Two-dimensional plots of bounce-averaged pitch angle scattering rates $< D_{\alpha\alpha} >$ as a function of electron kinetic energy $E_k$ and equatorial pitch angle due to **(d)** chorus, **(e)** plasmaspheric hiss, and **(f)** $He^+$-band EMIC waves.

itation loss of MeV electrons, scattering by hiss in plasmaspheric plumes may reduce the acceleration of MeV electrons by depleting the lower energy electron seed population (Summers et al., 2008; Jaynes et al., 2015). Scattering by electromagnetic ion cyclotron (EMIC) waves is an efficient contributor to the rapid removal of radiation belt relativistic electrons well above 1 MeV (e.g., Thorne and Kennel, 1971; Bortnik et al., 2006; Summers et al., 2007; Kersten et al., 2014). The electron loss timescales due to EMIC wave scattering can be shorter than a few minutes during the main phase of a storm. While $H^+$-band and $He^+$-band EMIC waves are most efficient in producing the pitch angle scattering loss of relativistic electrons at $\sim$ 1–2 MeV, it is $O^+$-band EMIC waves, when present, that dominate the scattering loss of 5–10 MeV electrons in the outer zone (Ni et al., 2015).

Figure 10 shows the Van Allen Probes EMFISIS WFR observations of chorus and hiss, and MAG observations of EMIC waves during the flux dropout period. Before the dynamic pressure pulse, all three wave modes were weak. When the $P_{dyn}$ enhancements occurred, as labeled in Fig. 10, chorus and EMIC waves were enhanced quickly during the storm main phase, and enhanced hiss emissions were observed later. The overall profiles of the three wave modes in Fig. 10 indicate that resonant wave-particle interactions could indeed take place during the period of the dynamic pressure pulse and the course of the geomagnetic storm. In order to quantitatively evaluate the roles of various plasma waves in driving the electron losses, we concentrate on the representative measurements of the three wave modes and compute the wave-induced scattering rates of radiation belt electrons, the results of which are shown in Fig. 11. Figure 11a–c display the measured power spectral intensities of chorus, hiss, and EMIC waves, respectively. It indicates that lower band chorus was very strong while hiss and $He^+$-Band EMIC waves had relatively smaller amplitudes during the storm time right after the $P_{dyn}$ pulse. The Full Diffusion Code (FDC) (Ni et al., 2008, 2011, 2015; Shprits and Ni, 2009) is used to quantify the bounce-averaged pitch angle diffusion rates due to lower band chorus, hiss, and $He^+$-Band EMIC waves. The background magnetic field is assumed to be dipolar, and electron density is derived from the upper hybrid frequency observed by Van Allen Probes EMFISIS instrument. Since the observation results show that the wave normal angles of all three wave emissions were quite small (not shown here), parallel or quasi-parallel propagation assumption is adopted for computations. In addition, following the previous studies (Meredith et al., 2003; Summers et al., 2007; Ni et al., 2015), we use the ion concentrations with $\eta_1 = 0.7$, $\eta_2 = 0.2$, $\eta_3 = 0.1$, (where $\eta_1$, $\eta_2$ and $\eta_3$ are the hydrogen, helium, and oxygen ion concentrations, respectively) to calculate the pitch angle scattering rates due to $He^+$-Band EMIC waves. The bounce-averaged pitch angle diffusion coefficients for the three wave emissions are shown in the right panels of Fig. 11 as a function of equatorial pitch

angle and electron energy. It is clearly shown that comparatively chorus waves could cause efficient pitch angle scattering of $\sim 10$ keV to $\sim 1$ MeV electrons at a rate of the order $10^{-3}$ s$^{-1}$ near the loss cone, which corresponds to small loss timescales (in other words, electron lifetimes) on the order of tens of minutes. We note that whistler-mode chorus can also play a significant role in electron acceleration (e.g., Horne et al., 2005; Thorne et al., 2013), while its net effect as either loss or energization (of 100s keV to MeV) depends on a number of factors (including EMIC waves, existing electrons' energy spectrum, wave properties, and so on). In addition, scattering by plasmaspheric hiss and $He^+$-band EMIC waves could result in the precipitation loss of relativistic (> 1 MeV) electrons on a timescale of days. But it becomes difficult for these plasma waves to scatter electrons at large equatorial pitch angles via gyroresonance. Therefore, there should be some underlying mechanism(s) accounting for the electron loss near and at 90° of pitch angles. Besides the outward radial diffusion, another possible mechanism can be that parallel acceleration by magnetosonic waves decreases the electron pitch angles and then facilitates wave induced electron scattering at lower pitch angles (e.g., Chen et al., 2015; Li et al., 2016). In this paper, we only make rough calculations for three popular wave modes and give some hints of the loss mechanisms. Overall, electron scattering by the three wave modes alone or combined can be proposed as an important mechanism to trigger the real electron losses in the outer zone. The precise analysis of wave-particle interaction needs global distributions of various plasma waves, which is outside the scope of the present study and left as a future study.

## 5 Conclusions

The present study is dedicated to a detailed investigation of the behaviors of the radiation belt electron flux dropout in response to two intense solar wind dynamic pressure enhancements on 2 October 2013. The simultaneous flux measurements from a cluster of 14 satellites with a broad spatial coverage manifest a strong dependence of storm-time outer zone electron flux evolution on the specific interplanetary and magnetospheric conditions, from which the losses through the magnetopause and to the atmosphere are registered. The main conclusions are summarized as follows:

1. When the intense dynamic pressure pulse occurred, the effects of magnetopause shadowing and atmospheric loss could take effect concurrently to contribute to the generation of an electron flux dropout;

2. Losses through the magnetopause were efficient and significant at $L \gtrsim 5$, which was captured clearly in response to the inward intrusion of the magnetopause location. The resultant sharp negative gradient in electron distribution at large $L$ shells contributed to enhanced losses at lower $L$ shells that could result from the outward radial diffusion;

3. Losses to the atmosphere were directly identified from the precipitating electron flux observations and from large decreases in outer zone trapped electron fluxes, to which pitch angle scattering by plasma waves could be a viable contributor;

4. Substorm injections and convection strongly enhanced the energetic electron fluxes up to hundreds of keV, which could delay other than avoid the occurrence of electron flux dropout at these energies for the intense dynamic pressure pulse.

## Data availability

For this study, Van Allen Probes REPT/MagEIS and EMFISIS data are from http://www.rbsp-ect.lanl.gov/science/DataDirectories.php and http://emfisis.physics.uiowa.edu/Flight/, respectively. THEMIS SST data are from http://themis.stp.isas.jaxa.jp/data/themis/. GOES data are from http://satdat.ngdc.noaa.gov/sem/goes/. POES MEPED data are from ftp://satdat.ngdc.noaa.gov/sem/poes/. CSSWE REPTile data are available at: http://cdaweb.gsfc.nasa.gov/cdaweb/sp_phys/). FengYun data are available upon request to bbni@whu.edu.cn.

**The Supplement related to this article is available online at doi:10.5194/angeo-34-493-2016-supplement.**

*Acknowledgements.* This work was supported by the NSFC grants 41204120, 41474141, 41304130 and 41574160, from the Projects funded by China Postdoctoral Science Foundation (2013M542051 and 2014T70732), and from the Project Supported by the Specialized Research Fund for State Key Laboratories. Binbin Ni thanks China Meteorological Administration and National Space Science Center for providing FengYun flux data. The authors acknowledge Daniel Baker, J. Bernard Blake and the ECT team for providing Van Allen Probes REPT and MagEIS data and acknowledge Craig Kletzing and the EMIFISIS team for providing Van Allen Probes EMFISIS data. The authors also thank the reviewers for valuable comments and constructive suggestions.

The topical editor, C. Owen, thanks two anonymous referees for help in evaluating this paper.

## References

Angelopoulos, V.: The THEMIS Mission, Space Sci. Rev., 141, 5–34, doi:10.1007/s11214-008-9336-1, 2008.

Baker, D. N., Kanekal, S. G., Hoxie, V. C., Batiste, S., Bolton, M., Li, X., Elkington, S. R., Monk, S., Reukauf, R., Steg, S., Westfall, J., Belting, C., Bolton, B., Braun, D., Cervelli, B., Hubbell, K.,

Kien, M., Knappmiller, S., Wade, S., Lamprecht, B., Stevens, K., Wallace, J., Yehle, A., Spence, H. E., and Friedel, R.: The Relativistic Electron-Proton Telescope (REPT) instrument on board the Radiation Belt Storm Probes (RBSP) spacecraft: Characterization of Earth's radiation belt high-energy particle populations, Space Sci. Rev., 179, 337–381, doi:10.1007/s11214-012-9950-9, 2013.

Baker, D. N., Jaynes, A. N., Hoxie, V. C., Thorne, R. M., Foster, J. C., Li, X., Fennell, J. F., Wygant, J. R., Kanekal, S. G., Erickson, P. J., Kurth, W., Li, W., Ma, Q., Schiller, Q., Blum, L., Malaspina, D. M., Gerrard, A., and Lanzerotti, L. J.: An impenetrable barrier to ultrarelativistic electrons in the Van Allen radiation belts, Nature, 515, 186–190, doi:10.1038/nature13956, 2014.

Blake, J. B., Carranza, P. A., Claudepierre, S. G., Clemmons, J. H., Crain, W. R., Dotan, Y., Fennell, J. F., Fuentes, F. H., Galvan, R. M., George, J. S., Henderson, M. G., Lalic, M., Lin, A. Y., Looper, M. D., Mabry, D. J., Mazur, J. E., McCarthy, B., Nguyen, C. Q., O'Brien, T. P., Perez, M. A., Redding, M. T., Roeder, J. L., Salvaggio, D. J., Sorensen, G. A., Spence, H. E., Yi, S., and Zakrzewski, M. P.: The Magnetic Electron Ion Spectrometer (MagEIS) instruments aboard the Radiation Belt Storm Probes (RBSP) spacecraft, Space Sci. Rev., 179, 383–421, doi:10.1007/s11214-013-9991-8, 2013.

Bortnik, J., Thorne, R. M., O'Brien, T. P., Green, J. C., Strangeway, R. J., Shprits, Y. Y., and Baker, D. N..: Observation of two distinct, rapid loss mechanisms during the 20 November 2003 radiation belt dropout event, J. Geophys. Res., 111, A12216, doi:10.1029/2006JA011802, 2006.

Boyd, A. J., Spence, H. E., Claudepierre, S. G., Fennell, J. F., Blake, J. B., Baker, D. N., Reeves, G. D., and Turner, D. L.: Quantifying the radiation belt seed population in the March 17, 2013 electron acceleration event, Geophys. Res. Lett., 41, 2275–2281, doi:10.1002/2014GL059626, 2014.

Casadio, S. and Arino, O.: Monitoring the South Atlantic Anomaly using ATSR instrument series, Adv. Space Res., 48, 1056–1066, 2011.

Chen, L., Maldonado, A., Bortnik, J., Thorne, R. M., Li, J., Dai, L., and Zhan, X.: Nonlinear bounce resonances between magnetosonic waves and equatorially mirroring electrons, J. Geophys. Res.-Space, 120, 6514–6527, doi:10.1002/2015JA021174, 2015.

Chen, Y., Reeves, G. D., and Friedel, R. H. W.: The energization of relativistic electrons in the outer Van Allen radiation belt, Nat. Phys., 3, 614–617, doi:10.1038/nphys655, 2007.

Coordinated Data Analysis Web (CDAWeb): Cubesats, CSSWE REPTile data, Goddard Space Flight Center, Space Physics Data Facility, available at: http://cdaweb.gsfc.nasa.gov/cdaweb/sp_phys/), 2012.

Dessler, A. J. and Karplus, R.: Some effects of diamagnetic ring currents on Van Allen radiation, J. Geophys. Res., 66, 2289–2295, doi:10.1029/JZ066i008p02289, 1961.

Evans, D. S. and Greer, M. S.: Polar Orbiting Environmental Satellite Space Environment Monitor-2: Instrument descriptions and archive data documentation, NOAA Tech. Mem. 93, version 1.4, Space Weather Predict. Center, Boulder, CO, 2004.

Friedel, R. H. W., Reeves, G. D., and Obara, T.: Relativistic electron dynamics in the inner magnetosphere: A review, J. Atmos. Solar Terr. Phys., 64, 265–282, doi:10.1016/S1364-6826(01)00088-8, 2002.

Fok, M.-C., Horne, R. B., Meredith, N. P., and Glauert, S. A.: Radiation Belt Environment model: Application to space weather nowcasting, J. Geophys. Res., 113, A03S08, doi:10.1029/2007JA012558, 2008.

Green, J. C.: MEPED Telescope Data Processing Algorithm Theoretical Basis Document, Natl. Oceanic and Atmos. Admin. Space Environment Center, Boulder, CO, 2013.

Green, J. C., Onsager, T. G., O'Brien, T. P., and Baker, D. N.: Testing loss mechanisms capable of rapidly depleting relativistic electron flux in the Earth's outer radiation belt, J. Geophys. Res., 109, A12211, doi:10.1029/2004JA010579, 2004.

Hudson, M. K., Baker, D. N., Goldstein, J., Kress, B. T., Paral, J., Toffoletto, F. R., and Wiltberger, M.: Simulated magnetopause losses and Van Allen Probe flux dropouts, Geophys. Res. Lett., 41, 1113–1118, doi:10.1002/2014GL059222, 2014.

Hwang, J., Choi, E.-J., Park, J.-S., Fok, M.-C., Lee, D.-Y., Kim, K.-C., Shin, D.-K., Usanova, M. E., and Reeves, G. D.: Comprehensive analysis of the flux dropout during 7–8 November 2008 storm using multisatellite observations and RBE model, J. Geophys. Res.-Space, 120, 4298–4312, doi:10.1002/2015JA021085, 2015.

Horne, R. B., Thorne, R. M., Glauert, S. A., Albert, J. M., Meredith, N. P., and Anderson, R. P.: Timescale for radiation belt electron acceleration by whistler mode chorus waves, J. Geophys. Res.-Space, 110, A03225, doi:10.1029/2004JA010811, 2005.

Jaynes, A. N., Baker, D. N., Singer, H. J., Rodriguez, J. V., Loto'aniu, T. M., Elkington, S. R., Ali, A., Li, X., Kanekal, S. G., Claudepierre, S. G., Fennell, J. F., Li, W., Thorne, R. M., Kletzing, C. A., Spence, H. E., and Reeves, G. D.: Source and Seed Populations for Relativistic Electrons: Their Roles in Radiation Belt Changes, J. Geophys. Res., 120, 7240–7254, doi:10.1002/2015JA021234, 2015.

Kim, H.-J. and Chan, A. A.: Fully adiabatic changes in storm time relativistic electron fluxes, J. Geophys. Res., 102, 22107–22116, doi:10.1029/97JA01814, 1997.

Kersten, T., Horne, R. B., Glauert, S. A., Meredith, N. P., Fraser, B. J., and Grew, R. S.: Electron losses from the radiation belts caused by EMIC waves, J. Geophys. Res.-Space, 119, 8820–8837, doi:10.1002/2014JA020366, 2014.

Kletzing, C. A., Kurth, W. S., Acuna, M., MacDowall, R. J., Torbert, R. B., Averkamp, T., Bodet, D., Bounds, S. R., Chutter, M., Connerney, J., Crawford, D., Dolan, J. S., Dvorsky, R., Hospodarsky, G. B., Howard, J., Jordanova, V., Johnson, R. A., Kirchner, D. L., Mokrzycki, B., Needell, G., Odom, J., Mark, D., Pfaff, R., Phillips, J. R., Piker, C. W., Remington, S. L., Rowland, D., Santolik, O., Schnurr, R., Sheppard, D., Smith, C. W., Thorne, R. M., and Tyler, J.: The electric and magnetic field instrument suite and integrated science (EMFISIS) on RBSP, Space Sci. Rev., 179, 127–181, doi:10.1007/s11214-013-9993-6, 2013.

Lam, M. M., Horne, R. B., Meredith, N. P., Glauert, S. A., Moffat-Griffin, T., and Green, J. C.: Origin of energetic electron precipitation > 30 keV into the atmosphere, J. Geophys. Res., 115, A00F08, doi:10.1029/2009JA014619, 2010.

Li, J., Ni, B., Ma, Q., Xie, L., Pu, Z., Fu, S., Thorne, R. M., Bortnik, J., Chen, L., Li, W., Baker, D. N., Kletzing, C. A., Kurth, W. S., Hospodarsky, G. B., Fennell, J. F., Reeves, G. D., Spence, H. E., Funsten, H. O., and Summers, D.: Formation of energetic electron butterfly distributions by magnetosonic waves via Landau

resonance, Geophys. Res. Lett., doi:10.1002/2016GL067853, online first, 2016.

Li, W., Ni, B., Thorne, R. M., Bortnik, J., Green, J. C., Kletzing, C. A., Kurth, W. S., and Hospodarsky, G. B.: Constructing the global distribution of chorus wave intensity using measurements of electrons by the POES satellites and waves by the Van Allen Probes, Geophys. Res. Lett., 40, 4526–4532, doi:10.1002/grl.50920, 2013.

Li, X., Baker, D. N., Temerin, M., Cayton, T. E., Reeves, G. D., Christiansen, R. A., Blake, J. B., Looper, M. D., Nakamura, R., and Kanekal, S. G.: Multisatellite observations of the outer zone electron variation during the November 3–4, 1993, magnetic storm, J. Geophys. Res., 102, 14123–14140, doi:10.1029/97JA01101, 1997.

Li, X., Sarris, T. E., Baker, D. N., Peterson, W. K., and Singer, H. J.: Simulation of energetic particle injections associated with a substorm on August 27, 2001, Geophys. Res. Lett., 30, 1004, doi:10.1029/2002GL015967, 2002.

Li, X., Palo, S., Kohnert, R., Gerhardt, D., Blum, L., Schiller, Q., Turner, D., Tu, W., Sheiko, N., and Cooper, C. S.: Colorado student space weather experiment: Differential flux measurements of energetic particles in a highly inclined low Earth orbit, in: Dynamics of the Earth's Radiation Belts and Inner Magnetosphere, edited by: Summers, D., Mann, I. R., Baker, D. N., and Schulz, M., Geophys. Monogr. Ser., 199, 385–404, AGU, Washington, DC, doi:10.1029/2012GM001313, 2012.

Li, X., Palo, S., Kohnert, R., Blum, L., Gerhardt, D., Schiller, Q., and Califf, S.: Small mission accomplished by students – impact on space weather research, Space Weather, 11, 55–56, doi:10.1002/swe.20025, 2013a.

Li, X., Schiller, Q., Blum, L., Califf, S., Zhao, H., Tu, W., Turner, D. L., Gerhardt, D., Palo, S., Kanekal, S., Baker, D. N., Fennell, J., Blake, J. B., Looper, M., Reeves, G. D., and Spence, H.: First results from CSSWE CubeSat: Characteristics of relativistic electrons in the near-Earth environment during the October 2012 magnetic storms, J. Geophys. Res. Space Physics, 118, 6489–6499, doi:10.1002/2013JA019342, 2013b.

Lyons, L. R. and Thorne, R. M.: Equilibrium structure of radiation belt electrons, J. Geophys. Res., 78, 2142–2149, doi:10.1029/JA078i013p02142, 1973.

Mauk, B. H., Fox, N. J., Kanekal, S. G., Kessel, R. L., Sibeck, D. G., and Ukhorskiy, A.: Science objectives and rationale for the radiation belt storm probes mission, Space Sci. Rev., 179, 3–27, doi:10.1007/s11214-012-9908-y, 2012.

McIlwain, C. E.: Ring current effects on trapped particles, J. Geophys. Res., 71, 3623–3628, doi:10.1029/JZ071i015p03623, 1966.

Meredith, N. P., Thorne, R. M., Horne, R. B., Summers, D., Fraser, B. J., and Anderson, R. R.: Statistical analysis of relativistic electron energies for cyclotron resonance with EMIC waves observed on CRRES, J. Geophys. Res., 108, 1250, doi:10.1029/2002JA009700, 2003.

Meredith, N. P., Horne, R. B., Thorne, R. M., and Anderson, R. R.: Survey of upper band chorus and ECH waves: Implications for the diffuse aurora, J. Geophys. Res., 114, A07218, doi:10.1029/2009JA014230, 2009.

Meredith, N. P., Horne, R. B., Lam, M. M., Denton, M. H., Borovsky, J. E., and Green, J. C.: Energetic electron precipitation during high-speed solar wind stream driven storms, J. Geophys. Res., 116, A05223, doi:10.1029/2010JA016293, 2011.

Millan, R. M. and Thorne, R. M.: Review of radiation belt relativistic electron losses, J. Atmos. Sol. Terr. Phys., 69, 362–377, doi:10.1016/j.jastp.2006.06.019, 2007.

National Centers for Environmental Information (NOAA): GOES Space Environment Monitor Data & Plots, available at: http://satdat.ngdc.noaa.gov/sem/goes/data/, 2010.

National Centers for Environmental Information (NOAA): POES Space Environment Monitor Data & Plots, available at: ftp://satdat.ngdc.noaa.gov/sem/poes/, 2013.

Ni, B., Thorne, R. M., Shprits, Y. Y., and Bortnik, J.: Resonant scattering of plasma sheet electrons by whistler-mode chorus: Contribution to diffuse auroral precipitation, Geophys. Res. Lett., 35, L11103, doi:10.1029/2008GL034032, 2008.

Ni, B., Shprits, Y., Nagai, T., Thorne, R., Chen, Y., Kondrashov, D., and Kim, H.: Reanalyses of the radiation belt electron phase space density using nearly equatorial CRRES and polar-orbiting Akebono satellite observations, J. Geophys. Res., 114, A05208, doi:10.1029/2008JA013933, 2009a.

Ni, B., Shprits, Y. Y., Thorne, R. M., Friedel, R., and Nagai, T.: Reanalysis of relativistic radiation belt electron phase space density using multisatellite observations: Sensitivity to empirical magnetic field models, J. Geophys. Res., 114, A12208, doi:10.1029/2009JA014438, 2009b.

Ni, B., Thorne, R. M., Shprits, Y. Y., Orlova, K. G., and Meredith, N. P.: Chorus-resonant scattering of diffuse auroral electrons in nondipolar magnetic fields, J. Geophys. Res., 116, A06225, doi:10.1029/2011JA016453, 2011.

Ni, B., Shprits, Y. Y., Friedel, R., Thorne, R. M., Daae, M., and Chen, Y.: Responses of Earth's radiation belts to solar wind dynamic pressure variations in 2002 analyzed using multi-satellite data and Kalman filtering, J. Geophys. Res.-Space, 118, 4400–4414, doi:10.1002/jgra.50437, 2013a.

Ni, B., Bortnik, J., Thorne, R. M., Ma, Q., and Chen, L.: Resonant scattering and resultant pitch angle evolution of relativistic electrons by plasmaspheric hiss, J. Geophys. Res.-Space, 118, 7740–7751, doi:10.1002/2013JA019260, 2013b.

Ni, B., Li, W., Thorne, R. M., Bortnik, J., Green, J. C., Kletzing, C. A., and Soria-Santacruz Pich, M.: A novel technique to construct the global distribution of whistler mode chorus wave intensity using low-altitude POES electron data, J. Geophys. Res.-Space, 119, 5685–5699, doi:10.1002/2014JA019935, 2014a.

Ni, B., Bortnik, J., Nishimura, Y., Thorne, R. M., Li, W., Angelopoulos, V., Ebihara, Y., and Weatherwax, A. T.: Chorus wave scattering dayside diffuse auroral precipitation: A detailed case study, J. Geophys. Res.-Space, 119, 897–908, doi:10.1002/2013JA019507, 2014b.

Ni, B., Cao, X., Zou, Z., Zhou, C., Gu, X., Bortnik, J., Zhang, J., Fu, S., Zhao, Z., Shi, R., and Xie, L.: Resonant scattering of outer zone relativistic electrons by multiband EMIC waves and resultant electron loss time scales, J. Geophys. Res.-Space, 120, 7357–7373, doi:10.1002/2015JA021466, 2015.

Orlova, K. G. and Shprits, Y. Y.: Dependence of pitch-scattering rates and loss timescales on the magnetic field model, Geophys. Res. Lett., 37, L05105, doi:10.1029/2009GL041639, 2010.

RBSP-ECT Data Portal: Van Allen Probes REPT/MagEIS data, available at: http://www.rbsp-ect.lanl.gov/science/DataDirectories.php, 2012.

Reeves, G. D., McAdams, K. L., Friedel, R. H. W., and O'Brien, T. P.: Acceleration and loss of relativistic electrons during geomagnetic storms, Geophys. Res. Lett., 30, 1529, doi:10.1029/2002GL016513, 2003.

Rodger, C. J., Clilverd, M. A., Green, J. C., and Lam, M. M.: Use of POES SEM-2 observations to examine radiation belt dynamics and energetic electron precipitation into the atmosphere, J. Geophys. Res., 115, A04202, doi:10.1029/2008JA014023, 2010.

Shprits, Y. Y. and Ni, B.: Dependence of the quasi-linear scattering rates on the wave normal distribution of chorus waves. J. Geophys. Res., 114, A11205, doi:10.1029/2009JA014223, 2009

Shprits, Y. Y., Thorne, R. M., Friedel, R., Reeves, G. D., Fennell, J., Baker, D. N., and Kanekal, S. G.: Outward radial diffusion driven by losses at magnetopause, J. Geophys. Res., 111, A11214, doi:10.1029/2006JA011657, 2006.

Shprits, Y. Y., Daae, M., and Ni, B.: Statistical analysis of phase space density buildups and dropouts, J. Geophys. Res., 117, A01219, doi:10.1029/2011JA016939, 2012.

Shue, J. H., Chao, J. K., Fu, H. C., Russell, C. T., Song, P., Khurana, K. K., and Singer, H. J.: A new functional form to study the solar wind control of the magnetopause size and shape, J. Geophys. Res., 102, 9497–9511, 1997.

Spence, H. E., Reeves, G. D., Baker, D. N., Blake, J. B., Bolton, M., Bourdarie, S., Chan, A. A., Claudepierre, S. G., Clemmons, J. H., Cravens, J. P., Elkington, S. R., Fennell, J. F., Friedel, R. H. W., Funsten, H. O., Goldstein, J., Green, J. C., Guthrie, A., Henderson, M. G., Horne, R. B., Hudson, M. K., Jahn, J.-M., Jordanova, V. K., Kanekal, S. G., Klatt, B. W., Larsen, B. A., Li, X., MacDonald, E. A., Mann, I. R., Niehof, J., O'Brien, T. P., Onsager, T. G., Salvaggio, D., Skoug, R. M., Smith, S. S., Suther, L. L., Thomsen, M. F., and Thorne, R. M.: Science goals and overview of the Energetic Particle, Composition, and Thermal Plasma (ECT) Suite on NASA's Radiation Belt Storm Probes (RBSP) mission, Space Sci. Rev., 179, 311–336, doi:10.1007/s11214-013-0007-5, 2013.

Summers, D., Ni, B., and Meredith, N. P.: Timescales for radiation belt electron acceleration and loss due to resonant wave-particle interactions: 2. Evaluation for VLF chorus, ELF hiss, and electromagnetic ion cyclotron waves, J. Geophys. Res., 112, A04207, doi:10.1029/2006JA011993, 2007.

Summers, D., Ni, B., Meredith, N. P., Horne, R. B., Thorne, R. M., Moldwin, M. B., and Anderson, R. R.: Electron scattering by whistler-mode ELF hiss in plasmaspheric plumes, J. Geophys. Res., 113, A04219, doi:10.1029/2007JA012678, 2008.

The RBSP-EMFISIS Team: Van Allen Probes EMFISIS data, available at: http://emfisis.physics.uiowa.edu/Flight/, 2012.

The THEMIS Team: THEMIS SST data, available at: http://themis.stp.isas.jaxa.jp/data/themis/, 2008.

Thorne, R. M.: Radiation belt dynamics: The importance of wave–particle interactions, Geophys. Res. Lett., 37, L22107, doi:10.1029/2010GL044990, 2010.

Thorne, R. M. and Kennel, C. F.: Relativistic electron precipitation during magnetic storm main phase, J. Geophys. Res., 76, 4446–4453, doi:10.1029/JA076i019p04446, 1971.

Thorne, R. M., O'Brien, T. P., Shprits, Y. Y., Summers, D., and Horne, R. B.: Timescale for MeV electron microburst loss during geomagnetic storms, J. Geophys. Res., 110, A09202, doi:10.1029/2004JA010882, 2005.

Thorne, R. M., Ni, B., Tao, X., Horne, R. B., and Meredith, N. P.: Scattering by chorus waves as the dominant cause of diffuse auroral precipitation, Nature, 467, 943–946, 2010.

Thorne, R. M., Li, W., Ni, B., Ma, Q., Bortnik, J., Baker, D. N., Spence, H. E., Reeves, G. D., Henderson, M. G., Kletzing, C. A., Kurth, W. S., Hospodarsky, G. B., Turner, D., and Angelopoulos, V.: Evolution and slow decay of an unusual narrow ring of relativistic electrons near L $\sim$ 3.2 following the September 2012 magnetic storm, Geophys. Res. Lett., 40, 3507–3511, doi:10.1002/grl.50627, 2013a.

Thorne, R. M., Li, W., Ni, B., Ma, Q., Bortnik, J., Chen, L., Baker, D. N., Spence, H. E., Reeves, G. D., Henderson, M. G., Kletzing, C. A., Kurth, W. S., Hospodarsky, G. B., Blake, J. B., Fennell, J. F., Claudepierre, S. G., and Kanekal, S. G.: Rapid local acceleration of relativistic radiation-belt electrons by magnetospheric chorus, Nature, 504, 411–414, doi:10.1038/nature12889, 2013b.

Tsyganenko, N. A. and Sitnov, M. I.: Modelling the dynamics of the inner magnetosphere during strong geomagnetic storms, J. Geophys. Res., 110, A03208, doi:10.1029/2004JA010798, 2005.

Tu, W. and Li, X.: Adiabatic effects on radiation belt electrons at low altitude, J. Geophys. Res., 116, A09201, doi:10.1029/2011JA016468, 2011.

Turner, D. L., Shprits, Y., Hartinger, M., and Angelopoulos, V.: Explaining sudden losses of outer radiation belt electrons during geomagnetic storms, Nature Phys., 8, 202–212, doi:10.1038/nphys2185, 2012a.

Turner, D. L., Morley, S. K., Miyoshi, Y., Ni, B., and Huang, C.-L.: Outer Radiation Belt Flux Dropouts, in: Current Understanding and Unresolved Questions, edited by: D. Summers, Mann, I. R., and Baker, D. N., Geophysical Monograph Series, 199, 195–212, AGU, Washington, DC, doi:10.1029/2012GM001310, 2012b.

Turner, D. L., Angelopoulos, V., Morley, S. K., Henderson, M. G., Reeves, G. D., Li, W., Baker, D. N., Huang, C.-L., Boyd, A., Spence, H. E., Claudepierre, S. G., Blake, J. B., and Rodriguez, J. V.: On the cause and extent of outer radiation belt losses during the 30 September 2012 dropout event, J. Geophys. Res.-Space, 119, 1530–1540, doi:10.1002/2013JA019446, 2014a.

Turner, D. L., Angelopoulos, V., Li, W., Bortnik, J., Ni, B., Ma, Q., Thorne, R. M., Morley, S. K., Henderson, M. G., Reeves, G. D., Usanova, M., Mann, I. R., Claudepierre, S. G., Blake, J. B., Baker, D. N., Huang, C.-L., Spence, H., Kurth, W., Kletzing, C., and Rodriguez, J. V.: Competing source and loss mechanisms due to wave-particle interactions in Earth's outer radiation belt during the 30 September to 3 October 2012 geomagnetic storm, J. Geophys. Res.-Space, 119, 1960–1979, doi:10.1002/2014JA019770, 2014b.

Wang, X., Wang, C., Yang, X., and Wang, S.: Comparison first result of space particle detector of FY2D with GOES, Chinese J. Geophys., 51, 611–617, 2008 (in Chinese).

Wang, C., Zhang, X., Wang, S., Wang, Y., Liu, C., and Jin, T.: Comparison of high energy particles observation results between FY-3A satellite and NOAA series satellites, Chin. J. Space Sci., 30, 49–54, 2010.

Wang, C. Q., Zhang, X., Li, J., Huang, C., Zhang, X., Jing, T., Shen, G., Zhang, S., Cao, G., Sun, Y., Liang, J., Zhu, G., and Han, Ying: Cross-calibration of high energetic particles data – A case study between FY-3B and NOAA-17, Sci. China Tech. Sci., 56, 2668–2674, doi:10.1007/s11431-013-5375-2, 2013.